

Effect of Yttrium Doping in Barium Zirconium Titanate Ceramics: A Structural, Impedance, and Modulus Spectroscopy Study

TANMAYA BADAPANDA, LAÉCIO SANTOS CAVALCANTE,
GERALDO EDUARDO DA LUZ Jr., NOUGA CARDOSO BATISTA,
SHAHID ANWAR, and ELSON LONGO

In the current article, we studied the effect of yttrium [Y^{3+}] ions' substitution on the structure and electric behavior of barium zirconate titanate (BZT) ceramics with a general formula $[Ba_{1-x}Y_{2x/3}](Zr_{0.25}Ti_{0.75})O_3$ (BYZT) with $[x = 0, 0.025, \text{ and } 0.05]$ which were prepared by the solid-state reaction method. X-ray diffraction patterns indicate that these ceramics have a single phase with a perovskite-type cubic structure. Rietveld refinement data confirmed $[BaO_{12}]$, $[ZrO_6]$, $[TiO_6]$, and $[YO_6]$ clusters in the cubic lattice. The Y^{3+} ions' effects on the electric conductivity behavior of BZT ceramics as a function of temperature and frequency are described, which are based on impedance spectroscopy analyses. The complex impedance plots display a double semicircle which highlights the influences of grain and grain boundary on the ceramics. Impedance analyses showed that the resistance decreased with the increasing temperature and resulted in a negative temperature coefficient of the resistance property in all compositions. Modulus plots represent a non-Debye-type dielectric relaxation which is related to the grain and grain boundary as well as temperature-dependent electric relaxation phenomenon and an enhancement in the mobility barrier by Y^{3+} ions. Moreover, the electric conductivity increases with the replacement of Ba^{2+} by Y^{3+} ions may be due to the rise in oxygen vacancies.

DOI: 10.1007/s11661-013-1770-3

© The Minerals, Metals & Materials Society and ASM International 2013

I. INTRODUCTION

BARIUM zirconate titanate $BaZr_xTi_{1-x}O_3$ (BZT) ceramics are among the most studied ferroelectric materials with various potential electronic applications such as piezoelectric transducers, dynamic random access memory (DRAM), and tunable microwave devices, as well as electric energy storage units.^[1–9] Because of their high dielectric constants, they are generally adopted for X7R multilayer ceramic capacitors (MLCCs). Removal of impurities and addition of doping in BZT ceramics are common ways to improve electric performance.^[10] Rare-earth oxide is an important additive for MLCCs with base metal electrodes.^[11] Trivalent rare-earth cations can behave as acceptors or donors depending on the site they occupy; the resulting electric properties will strongly depend on the size of the impurity cations.^[12,13] The research literature confirms

that a rare-earth element combined with magnesium ions are dominant additives in forming a shell and the core-shell structure in barium titanate ($BaTiO_3$) ceramics.^[14] Rare-earth elements are known to exhibit useful functions for stabilizing the temperature dependence of a relative dielectric constant and lowering the dissipation factor in dielectric ceramics.^[15,16] While the literature contains many reports on the electric behavior of rare-earth-modified $BaTiO_3$ ceramics, there is a dearth of reports on rare-earth-doped BZT ceramics. In the literature,^[17–21] few reports are available on the dielectric behavior study of different heterovalent substitutions such as yttrium [Y^{3+}] ions in BZT ceramics.

Again, interior defects such as A-site vacancies seriously influence ionic conductivity of ceramic materials.^[22–24] Thus, a fundamental understanding of the conduction mechanism due to the lattice defects created at short and medium ranges is imperative.^[25] These defects may also be responsible for dielectric relaxations in the high-temperature range. A complex impedance and modulus analysis is a powerful tool to separate grain boundary and grain-electrode effects which usually act as trap sites for defects.^[26]

Therefore, the current article contains a detailed explanation regarding the effect of the replacement of Ba^{2+} by Y^{3+} ions in the BZT system with the general stoichiometric formula $[Ba_{1-x}Y_{2x/3}](Zr_{0.25}Ti_{0.75})O_3$ (BYZT) ceramics with $[x = 0, 0.025, \text{ and } 0.05]$. Their structural and electric properties were investigated by X-ray diffraction (XRD), Rietveld refinement data, dielectric relaxation, and ac impedance spectroscopy

TANMAYA BADAPANDA, Ph.D. Scientist, is with the Department of Physics, CV Raman College of Engineering, Bhubaneswar 752054, India. LAÉCIO SANTOS CAVALCANTE, Ph.D. Scientist, GERALDO EDUARDO DA LUZ Jr., and NOUGA CARDOSO BATISTA, Professors, are with the Universidade Estadual do Piauí, CCN-Química, R. João Cabral, P.O. Box 2231, Teresina, PI 64002-150, Brazil. Contact e-mail: laeiosc@gmail.com SHAHID ANWAR, Ph.D. Scientist, is with the Colloids and Materials Chemistry, Institute of Minerals and Materials Technology, Bhubaneswar 751013, Odisha, India. ELSON LONGO, Professor, is with the LIEC-Universidade Estadual Paulista, P.O. Box 355, 14801-907 Araraquara, SP, Brazil.

Manuscript submitted February 8, 2013.

Article published online May 9, 2013

analyses. The main objective of this research is to find a suitable BaTiO₃-based material as a potential candidate for application as a thermistor device.

II. EXPERIMENTAL DETAILS

A. Synthesis of $[Ba_{1-x}Y_{2x/3}](Zr_{0.25}Ti_{0.75})O_3$ Ceramics Obtained by the Solid-State Reaction Method

BYZT ceramics with $[x = 0, 0.025, \text{ and } 0.05]$ were prepared by the solid-state reaction method. In the current synthesis, barium carbonate (BaCO₃) (99.9 pct, E. Merck India Ltd.), titanium oxide (TiO₂) (99.9 pct, E. Merck India Ltd.), zirconium oxide (ZrO₂) (99.9 pct, E. Merck India Ltd.), and yttrium oxide (Y₂O₃) (99.9 pct E. Merck India Ltd.) were used as raw materials. Using isopropyl alcohol (IPA), these compounds were stoichiometrically mixed and milled with an agate mortar to obtain homogenous ceramics. These ceramics were then heat treated at 1623 K (1350 °C) for 4 hours in a conventional furnace.

B. Characterizations

These BYZT ceramics were structurally characterized by XRD using a D/Max-2000PC diffractometer (Rigaku, Japan) with Cu K α radiation ($\lambda = 1.5406 \text{ \AA}$) in the 2θ range from 20 to 75 deg in the normal routine with a scanning velocity of 3 deg/min and from 20 to 110 deg at a scanning rate of 2 °C/min in the Rietveld refinement routine.

To measure electric properties of BYZT ceramics, disks were pressed uniaxially at 200 MPa; 2 wt pct polyvinyl alcohol was added as a binder. These disks were then sintered at 1673 K (1400 °C) for 4 hours. Silver contacts were deposited on the opposite disk faces and heated at 973 K (700 °C) for 5 minutes. Dielectric measurements were carried out in the frequency range from 1 kHz to 1 MHz using an LCR tester (Hioki, Japan) connected to a computer. Dielectric data were collected at an interval of 3 K (−270 °C); the heating rate was maintained at 0.5 K/min.

III. RESULTS AND DISCUSSION

A. XRD Patterns Analyses

Figure 1 illustrates XRD patterns of BYZT ceramics with different compositions: (a) $x = 0$, (b) $x = 0.025$, and (c) $x = 0.05$.

XRD patterns indicate that all BYZT ceramics are monophasic with a perovskite-type cubic structure and a space group ($Pm\bar{3}m$). All diffraction peaks are in good agreement with the respective Inorganic Crystal Structure Database (ICSD) card No. 88533.^[27] No secondary phase was detected at long range, which suggests that Y³⁺ ions were completely incorporated into the BYZT lattice. According to Shan *et al.*,^[28] the substitution of Ba²⁺ ion by Y³⁺ ions into A-sites causes distortions in the BZT cubic structure because of different atomic radii. Based on this information, we propose that the

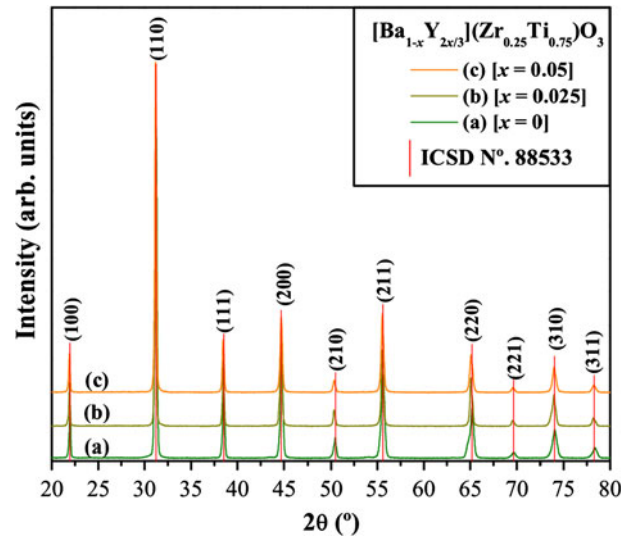
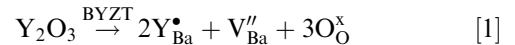


Fig. 1—XRD patterns of $[Ba_{1-x}Y_{2x/3}](Zr_{0.25}Ti_{0.75})O_3$ ceramics with [(a) $x = 0$, (b) 0.025, and (c) 0.05].

substitution of Ba atoms by Y atoms at A-sites causes an electronic compensation through the formation of barium vacancies (V''_{Ba}). Hence, the processes of cuboctahedral $[BaO_{12}]$ clusters substitution by distorted octahedral $[YO_6]$ clusters can be described by the following Kröger–Vink notation in Eq. [1]:



The above equation implies that every two Y³⁺ ions positioned on the A-site result in the formation of V''_{Ba} vacancies. In the current case, the electronic charge compensation occurs by the replacement of three Ba²⁺ ions by two Y³⁺ ions. However, when Y³⁺ ion content increases within the lattice because of the replacement of cuboctahedral $[BaO_{12}]$ clusters by distorted octahedral $[YO_6]$ clusters, an oxygen excess into the BYZT lattice occurs.

B. Rietveld Refinement Analyses

Figures 2(a) through (c) illustrate the structural refinement plot and 2D XRD multiplet (residuals) which are indicated by colors for BYZT ceramics with different compositions: (a) $x = 0$, (b) $x = 0.025$, and (c) $x = 0.05$.

The results obtained by the Rietveld refinement method indicate good agreement between observed XRD patterns and theoretical results. Moreover, the differences between the experimental XRD profile patterns observed and theoretical calculated data display small differences close to zero in the scale of intensity as illustrated by a line ($Y_{Obs} - Y_{Calc}$). 2D XRD multiplets (residuals) are indicated by colors (Figures 2(a) through (c)). In the current study, we initially applied the Rietveld method or full pattern analysis for the structural refinement of BYZT ceramics. The Rietveld method is a least-squares refinement procedure where the experimental step-scanned values are adapted to

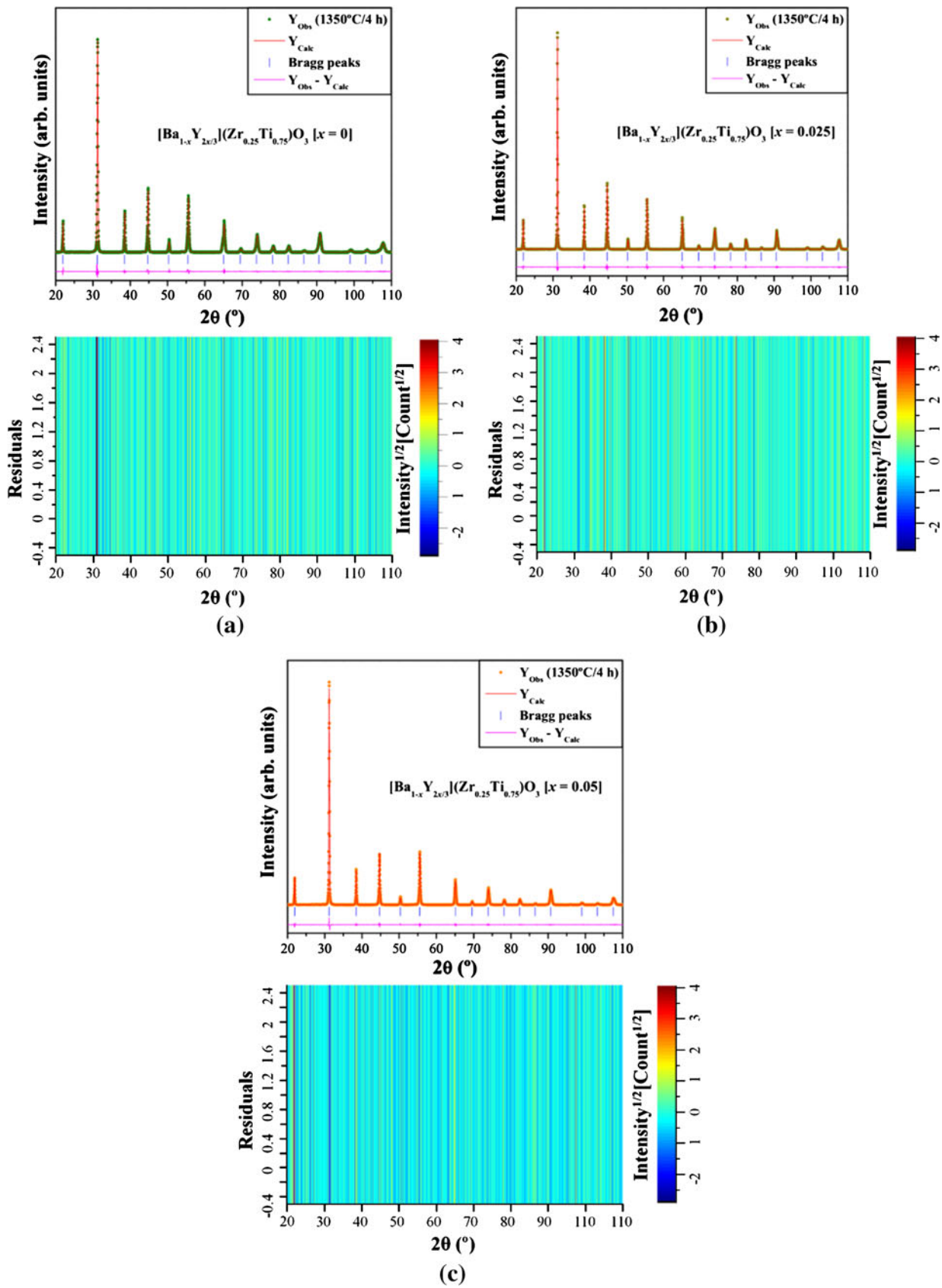


Fig. 2—Rietveld refinement plot and 2D multiplot (residuals) of $[\text{Ba}_{1-x}\text{Y}_{2x/3}](\text{Zr}_{0.25}\text{Ti}_{0.75})\text{O}_3$ ceramics with [(a) $x = 0$, (b) 0.025, and (c) 0.05].

calculated values. The profiles are considered to be known, and a model for a crystal structure is available.^[27] The observed experimental XRD pattern profiles of BYZT ceramics were refined with a theoretical line profile known as a Crystallographic Information File (CIF),^[29] which is related to the respective ICSD No. 88533.^[27]

Rietveld refinements performed using the MAUD program^[30] involved Rietveld texture and stress analysis.^[31] The optimized parameters were scale factor, background with exponential shift, exponential thermal shift, polynomial coefficients, basic phase, microstructure, crystal structure, microstrain, structure solution model, structure factor extractor, shift lattice constants, profile half-width parameters (u , v , w), texture, lattice parameters (a , b , c), and site occupancy factors (SOFs) (Wyckoff). These parameters were used to obtain a structural refinement with better quality and reliability.^[32,33] All Rietveld refinements for BYZT ceramics were performed based on a perovskite-type cubic structure and a space group ($Pm\bar{3}m$) with better approximation and indexing with a CIF file as indicated in ICSD card No. 88533.^[27] According to the literature,^[34] the quality of data from structural refinement is generally checked by R -values (R_{wnb} , R_b , R_{exp} , R_w , and σ), and therefore, the numbers obtained for R -values and σ can be easily checked.

The quality of the structural refinement data is acceptable when the R_w is <10 pct for a medium complex phase. For a high complex phase (monoclinic to triclinic), a value of $R_w < 15$ pct is acceptable; for a highly symmetric material or a compound (cubic) with few peaks, a value of $R_w < 8$ pct is acceptable. It is also important to verify σ values; therefore, good refinement

gives σ values lower than 2. In all cases, the experimental XRD pattern profiles for BYZT ceramics have σ values lower than 2. The results obtained from the Rietveld refinement are listed in Table I.

According to Table I, fitting parameters (R_{wnb} , R_b , R_{exp} , R_w , and σ) indicate good agreement between refined and observed XRD patterns for all BYZT ceramics with a cubic structure. This table also shows some variations in the values of the SOF due to replacement of Ba atoms by Y atoms. This behavior indicates that (Ba or Y) atoms located in the same A-site occupy the same site in a fractional percentage. Moreover, Rietveld refinement results obtained in the current study are in good agreement with results reported in the literature.^[35,36]

C. Supercell Representations with Cluster Modeling for $[Ba_{1-x}Y_{2x/3}](Zr_{0.25}Ti_{0.75})O_3$ Ceramics

Figures 3(a) and (b) show the schematic representation of crystalline supercells ($1 \times 2 \times 2$) for BYZT ceramics with (a) $x = 0$, and (b) $x = 0.025$ or 0.05 .

In these supercells, both Ti and Zr atoms (lattice formers) are bonded to six O atoms which form octahedral $[TiO_6]$ and $[ZrO_6]$ clusters (see Figures 3(a) and (b)). However, there is a distinct difference between these two clusters. In nonpolar or undistorted octahedral $[ZrO_6]$ clusters, Zr atoms are located in a centrosymmetric position in the octahedron. On the other hand, in the polar or distorted octahedral $[TiO_6]$ clusters, Ti atoms are slightly displaced along the $[001]$ direction (z -axis).^[37] This displacement or distortion can arise from the covalent character between the O-Ti-O bonds (directional orientations).^[38,39] Analyzing only

Table I. Lattice Parameters, Unit Cell Volume, c/a Ratio, and Atomic Positions for $[Ba_{1-x}Y_{2x/3}](Zr_{0.25}Ti_{0.75})O_3$ Ceramics with (A) $x = 0$ ■, (B) $x = 0.025$ ▲, and (C) $x = 0.05$ ●

Atoms	Wyckoff	Site	SOF	x	y	z	Occupancy
Panel A							
Ba	1a	$m\bar{3}m$	1	0	0	0	1
Ti	1b	$m\bar{3}m$	0.266	0.5	0.5	0.5	0.25
Zr	1b	$m\bar{3}m$	0.734	0.5	0.5	0.5	0.75
O1	3c	$mm2$	1	0.5	0.5	0	1
Panel B							
Ba	1a	$m\bar{3}m$	0.968	0	0	0	0.975
Y	1a	$m\bar{3}m$	0.032	0	0	0	0.025
Ti	1b	$m\bar{3}m$	0.257	0.5	0.5	0.5	0.25
Zr	1b	$m\bar{3}m$	0.743	0.5	0.5	0.5	0.75
O1	3c	$mm2$	1	0.5	0.5	0	1
Panel C							
Ba	1a	$m\bar{3}m$	0.937	0	0	0	0.95
Y	1a	$m\bar{3}m$	0.063	0	0	0	0.05
Ti	1b	$m\bar{3}m$	0.264	0.5	0.5	0.5	0.25
Zr	1b	$m\bar{3}m$	0.736	0.5	0.5	0.5	0.75
O1	3c	$mm2$	1	0.5	0.5	0	1

Panel A $Pm\bar{3}m(221)$ -cubic ($a = b = c = 4.0544 \text{ \AA}$; $c/a = 1$; $V = 66.65 \text{ \AA}^3$); [$x = 0$ ■]; $R_w = 7.95$ pct; $R_{\text{wnb}} = 6.15$ pct; $R_b = 5.38$ pct; $R_{\text{exp}} = 6.12$ pct; and $\sigma = 1.3$.

Panel B $Pm\bar{3}m(221)$ -cubic ($a = b = c = 4.0522 \text{ \AA}$; $c/a = 1$; $V = 66.54 \text{ \AA}^3$); [$x = 0.025$ ▲]; $R_w = 7.72$ pct; $R_{\text{wnb}} = 6.36$ pct; $R_b = 5.48$ pct; $R_{\text{exp}} = 5.11$ pct; and $\sigma = 1.51$.

Panel C $Pm\bar{3}m(221)$ -cubic ($a = b = c = 4.0503 \text{ \AA}$; $c/a = 1$; $V = 66.44 \text{ \AA}^3$); [$x = 0.05$ ●]; $R_w = 7.35$ pct; $R_{\text{wnb}} = 5.36$ pct; $R_b = 5.35$ pct; $R_{\text{exp}} = 5.42$ pct; and $\sigma = 1.35$.

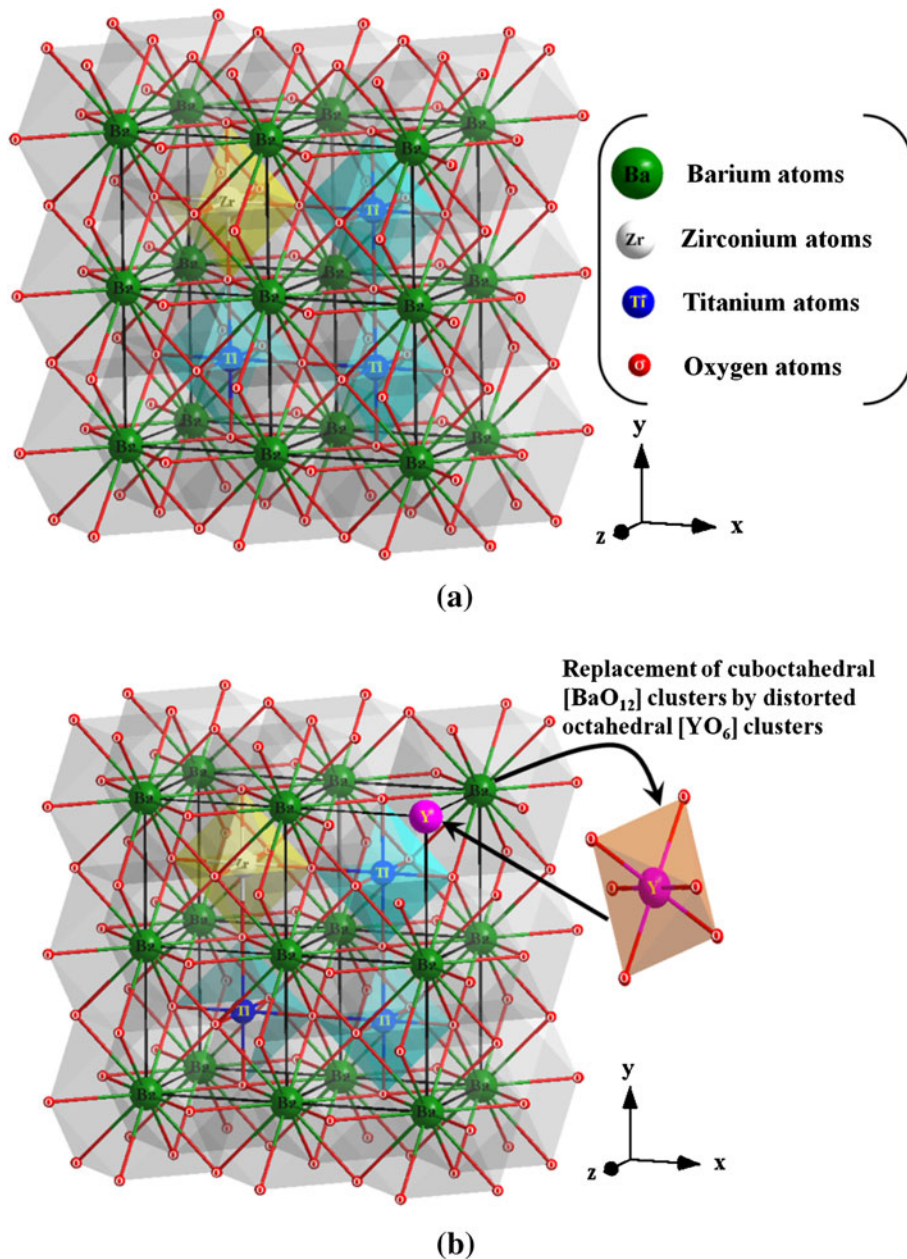


Fig. 3—Schematic representation of crystalline $[\text{Ba}_{1-x}\text{Y}_{2x/3}](\text{Zr}_{0.25}\text{Ti}_{0.75})\text{O}_3$ supercells ($1 \times 2 \times 2$) with [(a) $x = 0$, and (b) 0.025 or 0.05], illustrating the $[\text{TiO}_6]$, $[\text{ZrO}_6]$, $[\text{YO}_6]$, and $[\text{BaO}_{12}]$ clusters.

the lattice modifiers, each Ba atom is bonded to twelve O (radial orientations) atoms in a cuboctahedral configuration which forms $[\text{BaO}_{12}]$ clusters (see Figure 3(a)). According to the literature,^[9] the structural organizations as well as polarization mechanisms in the cubic BZT structures are related to polar or distorted $[\text{TiO}_6]$ clusters close to $[\text{BaO}_{12}]$ clusters. Figure 3(b) illustrates a crystalline lattice of BYZT ceramics with $x = 0.025$ or 0.05 , which is composed of supercells with four-type clusters. In the current research, we replaced Ba atoms with Y atoms at the A-site of the ABO_3 lattice which produced distorted octahedral $[\text{YO}_6]$ clusters instead of $[\text{BaO}_{12}]$ clusters.^[40]

D. Dielectric Properties' Analyses

Figure 4 shows dielectric constants (ϵ') and the dielectric loss ($\tan \delta$) of BYZT ceramics with different compositions: (a) $x = 0$, (b) $x = 0.025$, and (c) $x = 0.05$ which are shown as a function of the frequency at different temperatures.

In all compositions, the dielectric constant sharply decreases with the increasing frequency (<1 kHz), and the rate of decrease levels off at a certain frequency range (>100 kHz). Also, the dielectric constant decreases with the increasing Y^{3+} ion content. It is reported that the dielectric properties of the solid solutions were greatly influenced by the crystal structure

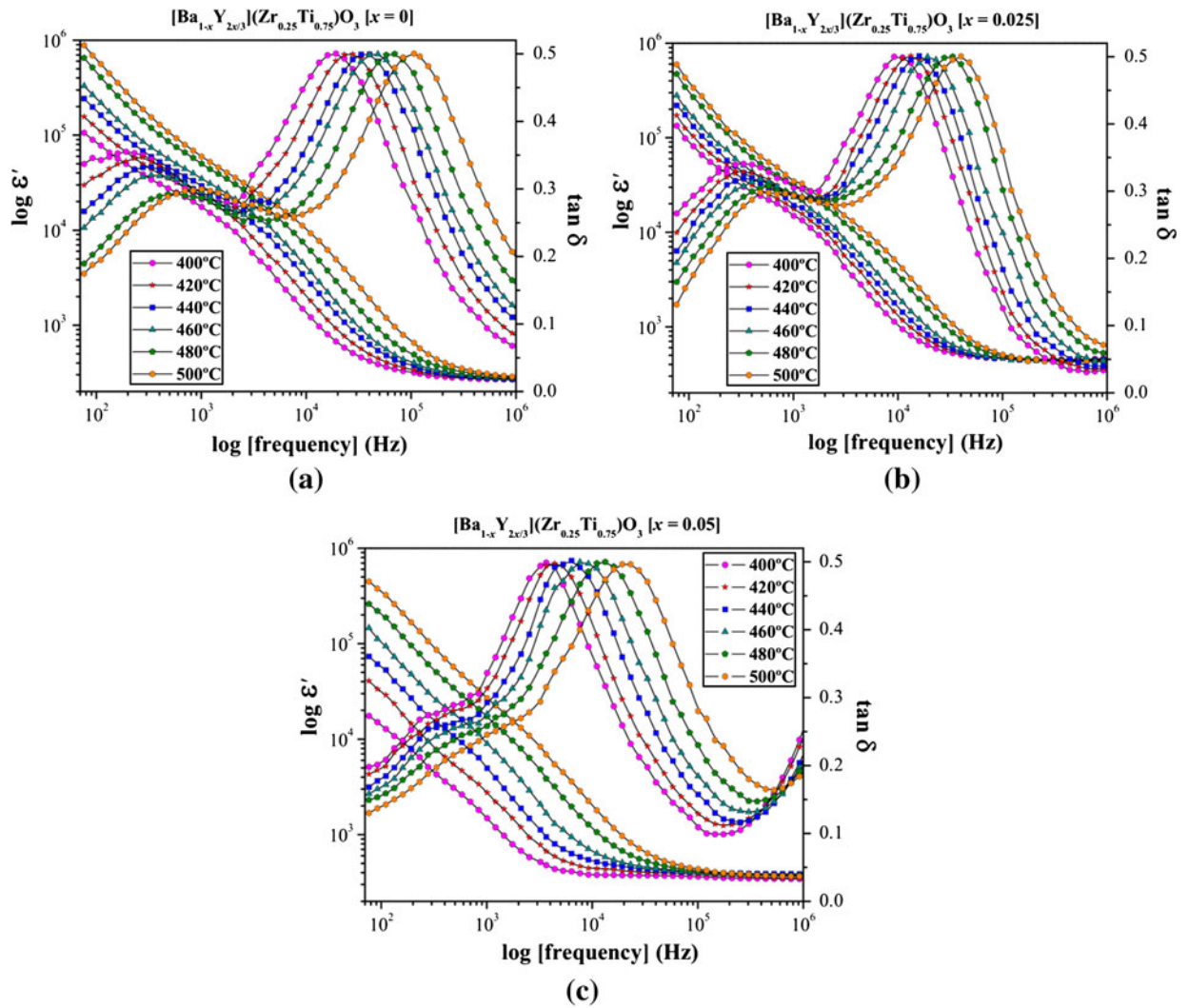


Fig. 4—Variation of real part of impedance: (a) ϵ' and (b) $\tan \delta$ for the $[\text{Ba}_{1-x}\text{Y}_{2x/3}](\text{Zr}_{0.25}\text{Ti}_{0.75})\text{O}_3$ ceramics with [(a) $x = 0$, (b) 0.025, and (c) 0.05] as a function of frequency at different temperatures.

and grain size. The substitution of a rare earth ion in the Ba-site decreases the internal strain, which results in the displacement of Ti^{4+} ions from octahedral centers, and hence the dielectric constant decreases.^[41]

The loss of dielectric constant with frequency at different temperatures shows two peaks superimposed on an apparent background, which increase with the measuring temperature but decrease with frequency. Peak positions apparently shift toward a higher frequency with increasing peak height when the temperature increases. This characteristic indicates that these peaks are associated with a thermally activated relaxation process. Losses below 100 Hz are directly proportional to the Y^{3+} ion content (x) and implies that loosely bounded oxygen vacancies may migrate to the grain boundary and thus may contribute to the space charge polarization. However, it is notable that peak losses shift to higher frequencies with increasing Y^{3+} ion content (x). Peaks are attributed to a reorientation of oxygen vacancies ($V_{\text{O}}^{\bullet\bullet}$) associated with cation defect

centers in the dipolar defect complex where $V_{\text{O}}^{\bullet\bullet}$ is the most mobile species.

E. Complex Impedance Spectroscopy Analyses

The variations of Z' and Z'' with frequencies at different temperatures of BYZT ceramics with different compositions: (a) $x = 0$, (b) $x = 0.025$, and (c) $x = 0.05$ are shown in Figures 5 (a) through (c).

These figures confirm that the value of Z' is larger in the low-frequency range and has a monotonous decrease with the rise in frequency which may be due to the ceramic polarization effect. The magnitude of Z' decreases with the increasing temperature which can be explained as a typical negative temperature coefficient of resistance (NTCR) behavior of BYZT ceramics (usually observed in semiconductors). In the high-frequency range, all curves merge at a very low value, so that Z' appears to become independent of both the frequency and temperature and indicates a possible

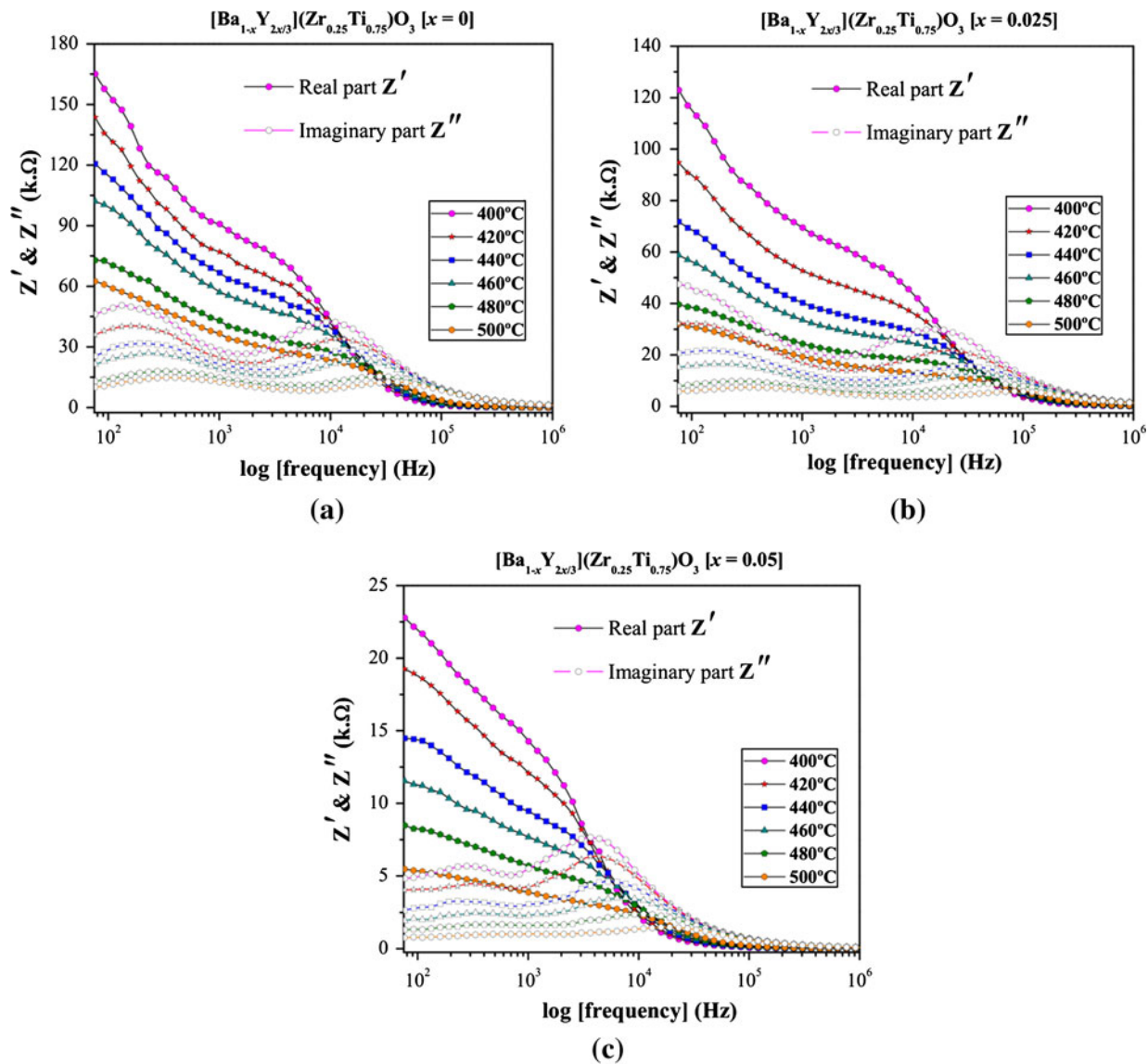


Fig. 5—Variation of real part Z' and imaginary part Z'' of $[\text{Ba}_{1-x}\text{Y}_{2x/3}](\text{Zr}_{0.25}\text{Ti}_{0.75})\text{O}_3$ ceramics with [(a) $x = 0$, (b) 0.025, and (c) 0.05] as a function of frequency at different temperatures.

release of a space charge. Moreover, the value of Z' is strongly dependent on the Y content of BYZT ceramics. The nature of the Z'' variation with frequency is characterized by (1) the appearance of peaks at a particular frequency for pure and Y-modified BZT; (2) a decrease in the peak height with the increasing the Y^{3+} ions concentration of BZT; (3) a significant peak with the increasing the Y^{3+} ions concentration; (4) a marked asymmetry in the peak pattern; and (5) a spectrum merger at higher frequencies irrespective of concentration. A peak broadening with a concentration change suggests a concentration-dependent relaxation process in the material. The asymmetric peak broadening suggests electric processes in the material with a relaxation time spread (as indicated by the peak width) at two equilibrium positions. Since these observations are made at higher temperatures, relaxation species such as defects may be responsible for electric conduction in the

material by hopping of electrons/oxygen ion vacancy/defects among the available localized sites. Peak heights of peaks decrease gradually with the increasing frequency as well as temperature. Finally, they merge in the high-frequency domain which indicates space charge polarization appearance at the lower frequency and its disappearance at a higher frequency.^[42] Peaks appearing in the symmetric pattern area and their positions appear to be shifting toward the higher-frequency side upon substitution of Y at the Ba site which is assumed during the calculation of charge component balancing in BYZT ceramics systems. The current result indicates that the electric process occurring in the material is initially slowed down on the Y^{3+} ions substitution because of an accumulation of the space charge. The spectrum merger in the high-frequency region irrespective of the Y^{3+} ions concentration reveals a space charge in the material which governs the electric process in the high-frequency

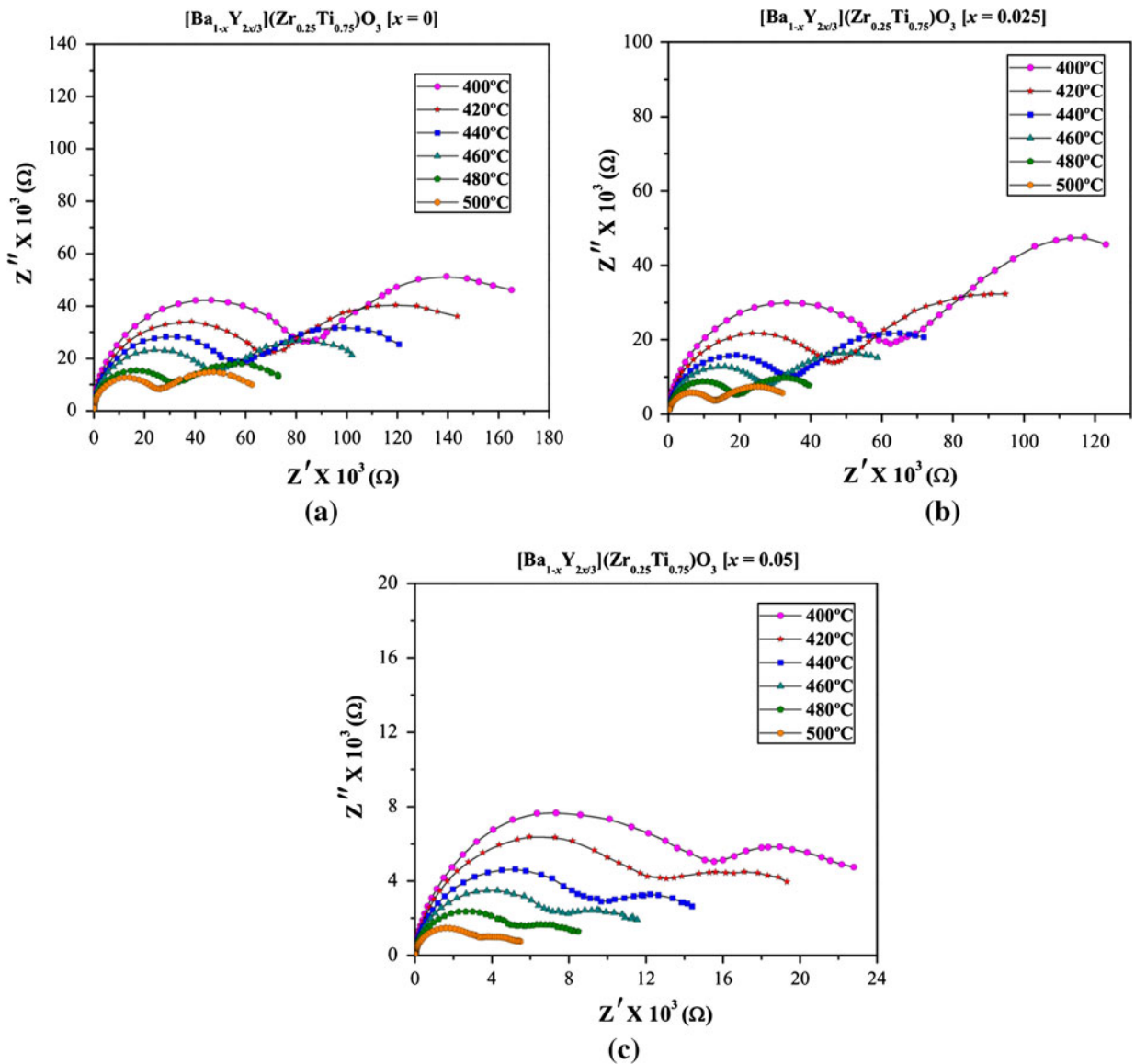


Fig. 6—Nyquist (Cole–Cole) plots between Z' and Z'' for $[\text{Ba}_{1-x}\text{Y}_{2x/3}](\text{Zr}_{0.25}\text{Ti}_{0.75})\text{O}_3$ ceramics with [(a) $x = 0$, (b) 0.025, and (c) 0.05] measured at various temperatures.

region. The peak shifting toward the high-frequency side is attributed to a phenomenon associated with a minimum capacitive effect on Y^{3+} ions doping. This shifting can possibly be caused by the net impedance enhancement of materials which thereby enhances their barrier properties on the Y^{3+} ion modification of BZT. The magnitude of Z'' corresponding to these peaks is strongly dependent on the Y^{3+} ion content in BYZT lattice. Therefore, based on the current results, it can be proposed that our ceramics can be applied like ceramic materials with potential for future application in NTC thermistor devices.

The Cole–Cole plot of BYZT ceramics is shown in Figures 6(a) through (c).

Figures 6(a) through (c) show two depressed semicircles which represent data taken at different temperatures in all compositions which exhibit both grain (bulk property) and grain boundary effects. The contribution

positioned at a low frequency corresponds to the grain boundary response; in the high frequency, it corresponds to the specific property of the bulk. All semicircles exhibit a degree of depression instead of a semicircle-centered real axis Z'' because of a relaxation time distribution. The depression of the semicircle is considered as further evidence of polarization phenomena with a relaxation time distribution (a non-Debye type of relaxation). This nonideal behavior can be correlated to several factors such as grain orientation, grain boundary, stress–strain phenomena, and atomic-defect distribution.

These types of depressed semicircles representing constant phase element (CPE) in the equivalent circuits are shown in Figure 7.

In solid materials, a relaxation time distribution is usually observed, and the capacitance is replaced by a CPE, which more accurately represents the behaviors of

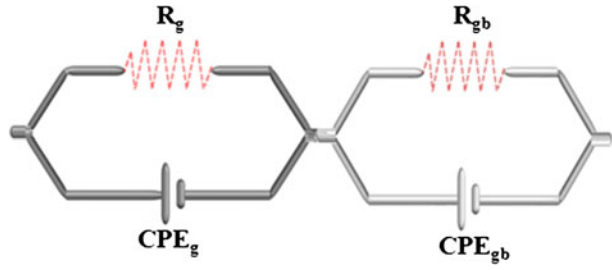


Fig. 7—Equivalent circuit of parallel R-CPE applied to stimulate the resistance and capacitance values from Nyquist plots.

the grain interior, grain boundary, and electrode processes.^[43] A CPE is characterized by two parameters. The admittance $Y(\omega)$ of CPE can be defined as follows:

$$Y^*(\omega) = A(j\omega)^P \quad [2]$$

where, the coefficient A relates to the size, thickness, and material properties of a ferroelectric capacitor; and P is the degree of energy dissipation. The CPE causes depression of the ideal semicircle which is observed on the complex plane plots by an angle:

$$\theta = (1 - P) \frac{\pi}{2} \quad [3]$$

where θ is the depression angle.

Separation of the bulk and grain boundary of the material is obtained by fitting the experimental response to the response of an equivalent circuit, which is usually considered to be composed of a series of two parallel resistor-CPE (R-CPE) elements (see Figure 7). After performing the impedance spectroscopy data simulation, calculated values of the equivalent electric circuit parameters were then related to the characteristic parameters of the (macroscopic) processes according to the following relations:^[44,45]

$$v_{\max} = \frac{1}{2\pi(RT)^{1/P}} \quad [4]$$

$$C = \frac{1}{2\pi R v_{\max}} \quad [5]$$

where v_{\max} is a relaxation frequency, R and C are, respectively, the resistance and capacitance of the bulk or grain boundary or electrode processes contributions to impedance data. Results of the data simulation in the form of estimated parameters of the relaxation processes are given in Table II.

The decrease of the resistance with the increasing Y^{3+} ion content in the BZT lattice is verified by the electric conduction enhancement with oxygen vacancies ($V_O^{\bullet\bullet}$).

The bulk resistance variation with temperature is illustrated in Figure 8.

Figure 8 illustrates that the resistance of the material decreases with the increasing temperature which results in NTCR behavior in the materials. The Y^{3+} -substituted BZT lattice behaved as a donor which created an energy level below the conduction band (CB). The

Table II. Simulated Parameters of Nyquist Plot by Equivalent Circuits at 733 K (460 °C) for $[\text{Ba}_{1-x}\text{Y}_{2x/3}](\text{Zr}_{0.25}\text{Ti}_{0.75})\text{O}_3$ Ceramics with $[x = 0 \blacksquare, x = 0.025 \blacktriangle, \text{ and } x = 0.05 \bullet]$

	BZT \blacksquare	BYZT \blacktriangle	BYZT \bullet
R_g (K Ω)	23.077	11.449	2.169
C_g (nF)	173.3	144.1	84.86
v_{\max} (Hz)	39816	96517	24835
θ_g	0 deg	4°46'2"	5°55'36"
R_{gb} (K Ω)	45.178	26.939	2.929
C_{gb} (nF)	8.683	17.17	2.189
v_{\max} (Hz)	405	344	865
θ_{gb}	24°11'24"	33°4'20"	27°45'41"
χ^2	0.00104	0.00025	0.00077

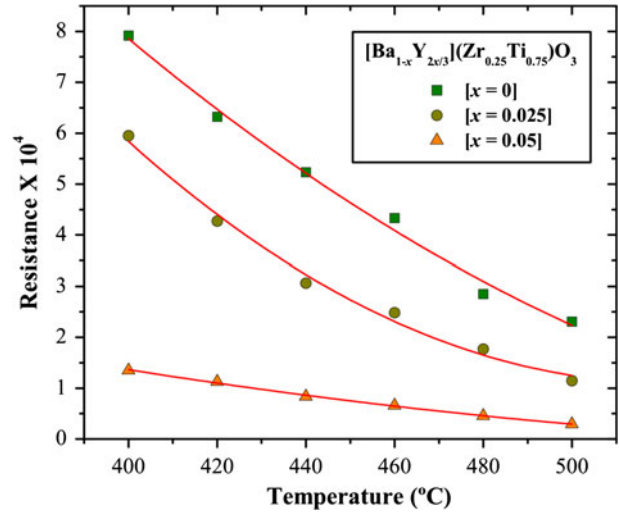


Fig. 8—Variation of bulk $[\text{Ba}_{1-x}\text{Y}_{2x/3}](\text{Zr}_{0.25}\text{Ti}_{0.75})\text{O}_3$ bulk ceramics resistance with different temperatures.

increase in the temperature provided sufficient thermal energy for these donor cations to move toward the CB. Thus, the resistivity of the samples reduced with the increasing temperature. The relationship between resistance and temperature for a compound exhibiting NTCR behavior is expressed as

$$R_T = R_N \exp \left[\beta \left(\frac{T_N - T}{TT_N} \right) \right] \quad [6]$$

where R_T is the resistance at temperature T , R_N is the resistance at temperature T_N known, and β is a NTC thermistor characteristic parameter.

The thermistor characteristic parameter can be expressed as shown in Eq. [7]:

$$\beta = \left[\frac{TT_N}{T_N - T} \right] \ln \frac{R_T}{R_N} \quad [7]$$

The thermistor sensitivity β can also be defined by the temperature coefficient of resistance (α) which can be expressed as a function of β parameter according to the literature^[46] by Eq. [8]:

$$\alpha = (1/R)[d(R)/dT] = -\beta/T^2 \quad [8]$$

From the Eq. [8], we calculated the (β) values in the temperature range from 673 K to 773 K (400 °C to 500 °C) as being equal to 3965.27, 5063.63, and 4972.85 for BYZT [$x = 0$], BYZT [$x = 0.025$], and BYZT [$x = 0.05$], respectively.

The α parameter values at 673 K and 773 K (400 °C and 500 °C) are equal to 2.47×10^{-2} and 1.87×10^{-2} for BYZT [$x = 0$]; 3.16×10^{-2} and 2.39×10^{-2} for BYZT [$x = 0.025$]; and 3.11×10^{-2} and 2.35×10^{-2} for BYZT [$x = 0.05$], respectively.

The B -constant value was calculated according to the literature^[47] by the standard formula presented in Eq. [9]:

$$B = \frac{\ln \frac{R_1}{R_2}}{\frac{1}{T_1} - \frac{1}{T_2}} \quad [9]$$

The B -constant values calculated from Eq. [9] are 2465, 306, and 3296 for BYZT ceramics with [$x = 0, 0.025, \text{ and } 0.05$], respectively. B -constant values reported here are superior to the values reported earlier by other researchers.^[48,49] Thus, the obtained B -values endorsed BYZT ceramics as a good quality NTC material for the fabrication of thermistor devices.

F. Complex Impedance Spectroscopy Analyses

The frequency–temperature dependences of the real part of the electric modulus (M') and the imaginary part of the modulus (M'') for BYZT ceramics with [$x = 0, 0.025, \text{ and } 0.05$] are shown in Figures 9(a) through (c).

These figures show that the modulus peaks shift toward the higher-frequency side with the increasing temperature. $M'(\omega)$ shows a dispersion tending toward

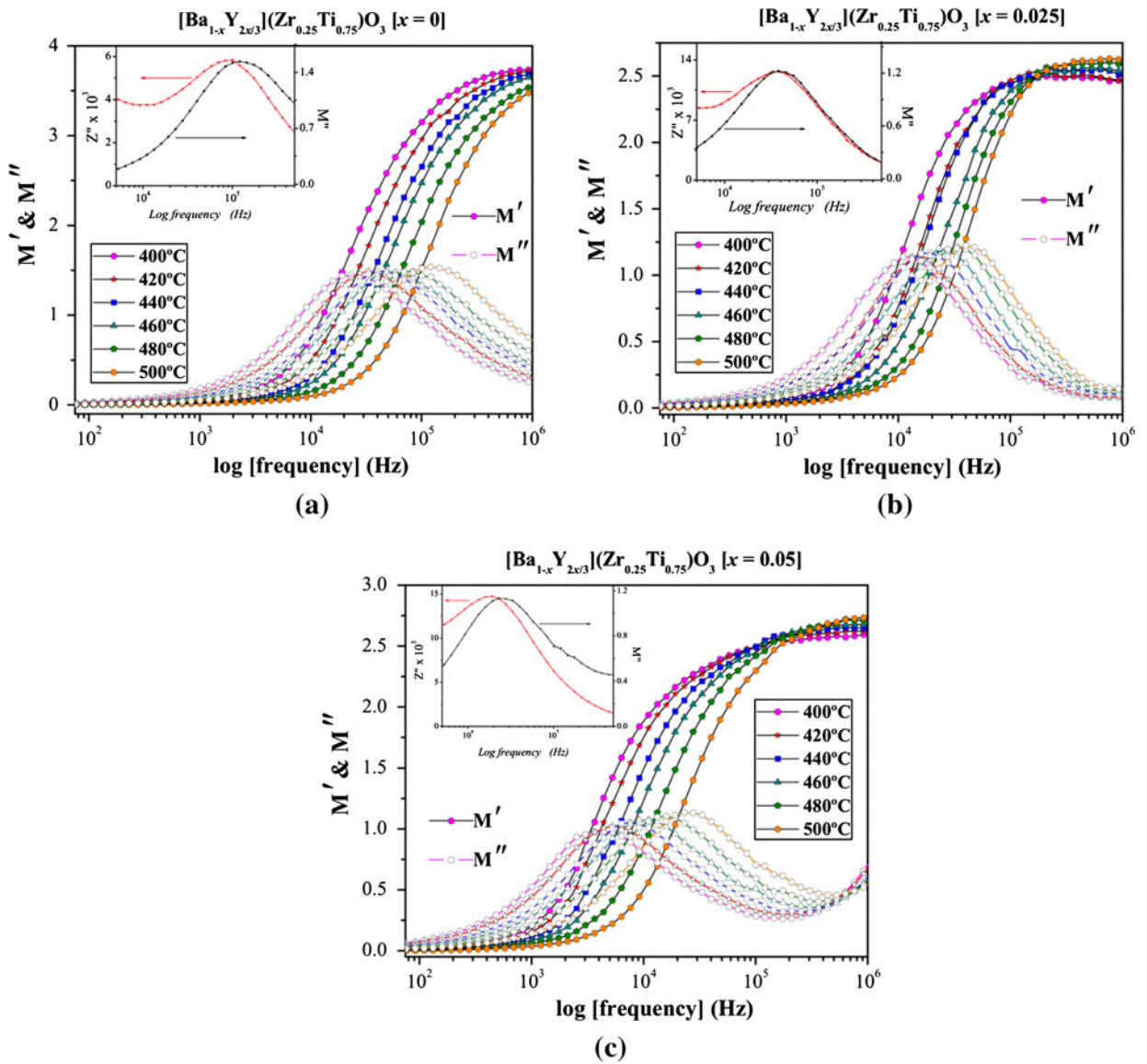


Fig. 9—Frequency–temperature dependences of the real part (M') and the imaginary part (M'') of modulus of $[\text{Ba}_{1-x}\text{Y}_{2x/3}](\text{Zr}_{0.25}\text{Ti}_{0.75})\text{O}_3$ ceramics with [(a) $x = 0$, (b) 0.025, and (c) 0.05]. Inset shows the combined analysis of frequency dependence Z'' and M'' at 773 K (500 °C).

M_∞ (the asymptotic value of $M'(\omega)$ at higher frequencies) which shows a very low value in the low-frequency region and a higher value in the high-frequency region because of continuous dispersion with increasing frequency. In the low-temperature region, the value of M' increases with the increase in frequency and decreases with the rise in temperature at a slow rate; in the high-temperature region, the value of M' increases rapidly with the increases in both the temperature and frequency which may contribute to conduction phenomena because of the short-range charge carrier mobility. This result implies the lack of a restoring force for the charge flow under the influence of a steady electric field.^[50]

Asymmetric modulus peaks shifts toward the higher-frequency side and exhibit the correlation between mobile charge carrier motions.^[51] The asymmetry in peak broadening shows the spread of relaxation times with a different time constant and hence non-Debye type relaxations. The existence of low-frequency peaks reveal

that ions can move over long distances, whereas high-frequency peaks suggest the confinement of ions due to the hopping mechanism in the electric conduction of materials.

The inset in Figures 9(a) through (c) shows the combined analysis of Z'' and M'' peaks at 773 K (500 °C) which helps us to distinguish whether a particular relaxation process in the material is due to

Table III. Activation Energies of Maximum Frequencies and Conductivities for $[\text{Ba}_{1-x}\text{Y}_{2x/3}](\text{Zr}_{0.25}\text{Ti}_{0.75})\text{O}_3$ Ceramics with $[x = 0 \blacksquare, x = 0.025 \blacktriangle, \text{ and } x = 0.05 \bullet]$

	$\omega_{\max} (Z''_{\max})$ (eV)	σ_g (eV)	σ_{gb} (eV)	$\omega_{\max} (M''_{\max})$ (eV)
BZT \blacksquare	0.429	0.338	0.377	0.396
BYZT \blacktriangle	0.502	0.446	0.516	0.502
BYZT \bullet	0.540	0.488	0.539	0.566

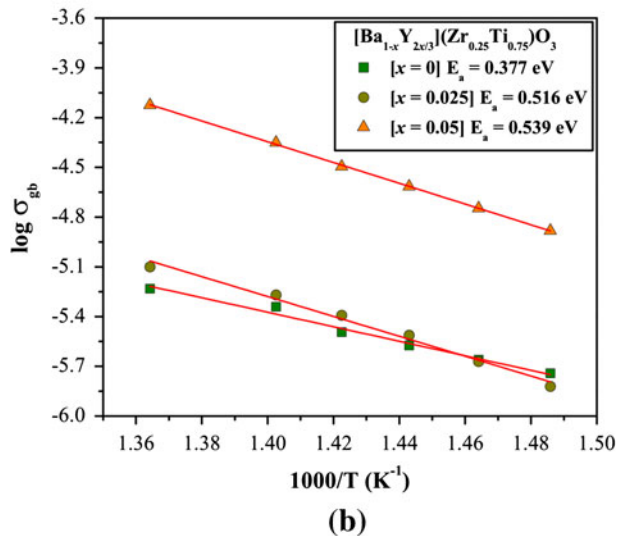
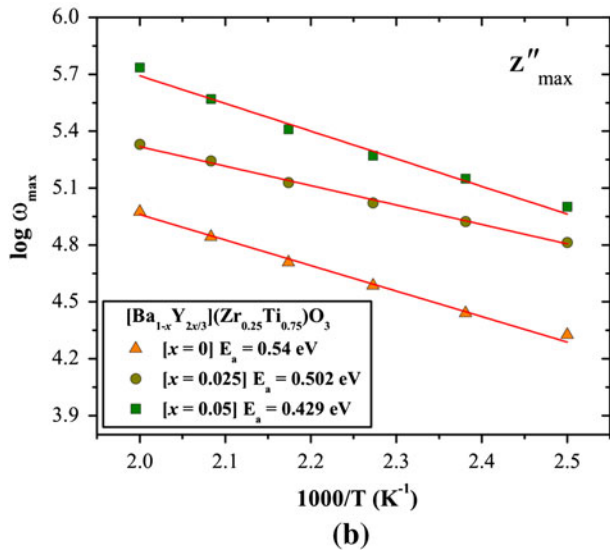
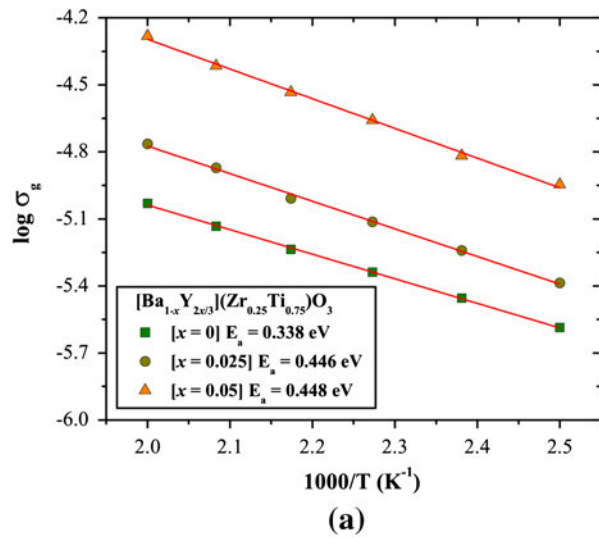
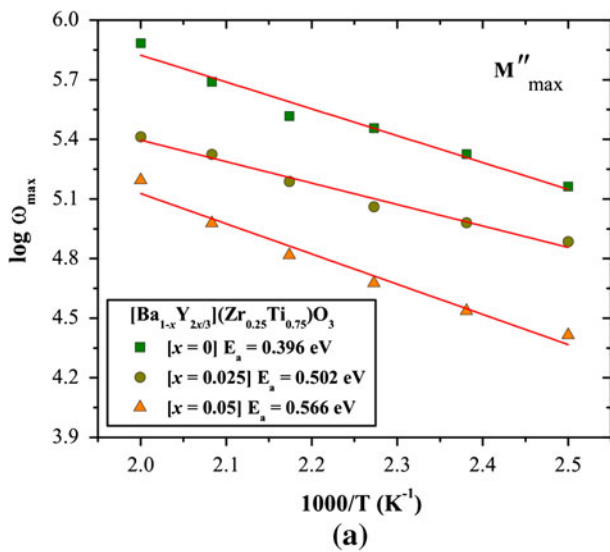


Fig. 10—(a) Arrhenius plots of maximum frequencies from $\log f$ vs Z'' and (b) Arrhenius plots of maximum frequencies from $\log f$ vs M'' at different temperatures.

Fig. 11—Arrhenius plot of $[\text{Ba}_{1-x}\text{Y}_{2x/3}](\text{Zr}_{0.25}\text{Ti}_{0.75})\text{O}_3$ ceramics with [(a) $x = 0$, (b) 0.025, and (c) 0.05] for: (a) grain conductivity and (b) grain boundary conductivity.

short-range or long-range charge carrier movements.^[52] Figures 9(a) through (c) show that deviations of maximum peak frequencies change with increasing concentrations of the Y^{3+} ions in the BZT lattice. Therefore, it can be concluded that the doped samples show short-range charge carrier movement, whereas undoped samples show long-range charge carrier movement.

The frequency ω_m (corresponding to Z''_{\max} and M''_{\max}) gives the most probable relaxation time τ_m from the condition $\omega_m\tau_m = 1$. The most probable relaxation time follows the Arrhenius law from Eq. [10] below:

$$\omega_m = \omega_0 \exp\left(\frac{-E_a}{k_B T}\right) \quad [10]$$

where ω_0 is the pre-exponential factor, and E_a is the activation energy.

Figures 10 (a) and (b) show a plot of the $\log \omega_m$ vs $10^3/T$ for Z'' and M'' , where the dots are experimental data and the solid line is the least-squares straight-line fit, respectively.

The activation energy (E_a) calculated from the least-squares fit to the points. The calculated values of the activation energy are presented in Table III.

Figures 11(a) and (b) illustrate a plot of the $\log \sigma_g$ and $\log \sigma_{gb}$ vs $10^3/T$, where the dots are experimental data and the solid line is the least-squares straight-line fit.

The E_a calculated values from the least-squares fit to the points for the grain and grain boundaries for the BYZT ceramics with $x = 0.025$ and 0.05 are greater than those for pure ceramics. The E_a calculated values are presented in Table III. The increase in the activation energy with the increasing Y^{3+} ion content may be due to the increase in oxygen vacancies. In Figures 10(a, b) and 11(a, b), the values found for the grain boundary

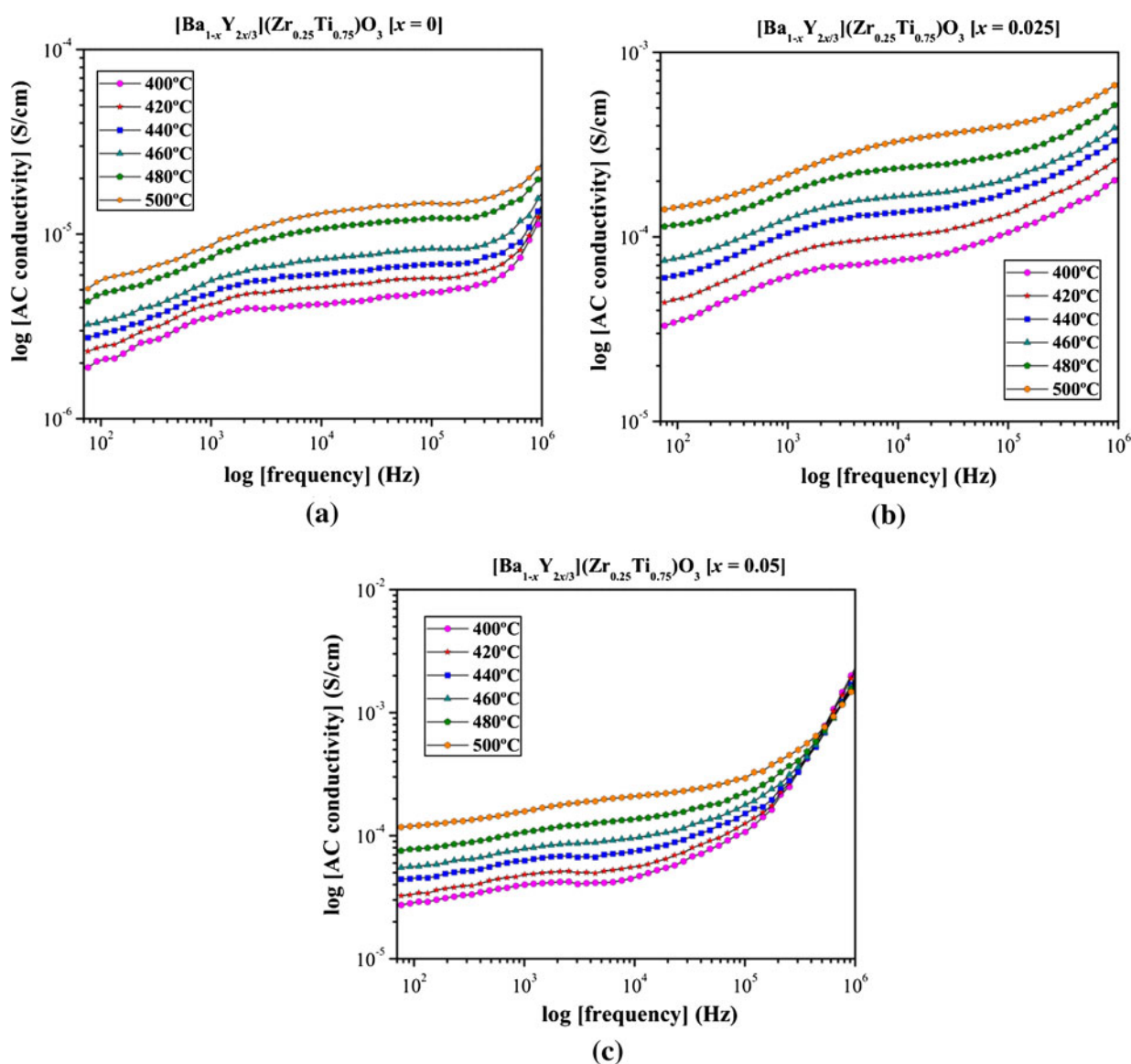


Fig. 12—Frequency dependences of ac conductivity for different temperatures of $[Ba_{1-x}Y_{2x/3}](Zr_{0.25}Ti_{0.75})O_3$ ceramics with [(a) $x = 0$, (b) 0.025 , and (c) 0.05].

are greater than those for the grain because of the difficulty of the electron mobility in the contour ceramic.

G. Conductivity Analyses

The electric conductivity frequency variations are shown in Figures 12(a–c).

There is a change in slope of the conductivity spectrum at a particular frequency which is conventionally known as the “hopping frequency (ω_p).” The square law conductivity dependence at higher frequencies has been explained by Argall and Jonscher^[53] based on the two-centered hopping. The value of AC conduction can easily be understood from the power law given by the equation: $\sigma(\omega) = A(T)\omega^n + \sigma(T)$, where $A(T)$ is a pre-exponential factor dependent on temperature; $\sigma(T)$ corresponds to the DC conductivity; and n is a constant which is a function of both temperature and frequency, and corresponds to short-range charge carriers through trap sites separated by energy barriers of varying heights. The conductivity dispersion at low frequency can be attributed to nonadiabatic hopping of charge carriers between impurity sites. The observed frequency-dependent conductivity behavior is due to the charge carrier hopping in frequency finite $[\text{BaO}_{12}] \dots [\text{YO}_6] \dots [\text{ZrO}_6] \dots [\text{TiO}_6]$ clusters. The conductivity jump indicates the enhancement in the mobile charge carrier through the grain boundary which supports the conclusion drawn from complex impedance spectra.

The bulk conductivities of the compound at higher temperatures are evaluated by means of impedance data using the relation $\sigma(T) = d/AR$ where ($R = R_b$ and R_{gb}) are the bulk and grain boundary resistances, d is the thickness, and A is the electrode area deposited on the sample. The conductivity variation indicates an increase of conductivity with the rising temperature with a typical Arrhenius-type behavior which has a linear dependence on the conductivity logarithm. The temperature-dependence type of DC conductivity indicates that the electric conduction in the material is a thermally activated process. The activation energy was calculated from the linear portion of the plot of DC conductivity (σ) vs $10^3/T$ (see Figures 12(a) and (b)). The activation energies calculated from the bulk and grain boundary effects are presented in Table III. In ceramic samples, usually oxygen vacancies are considered as one of the mobile charge carriers in perovskite-type ferroelectric.^[54] The ionization of oxygen vacancies creates conducting electrons, which are easily thermally activated. Conduction results and the activation energy conduction values suggest the possibility that the conduction in the high-temperature range of charge carriers may be due to oxygen vacancies.

IV. CONCLUSIONS

In summary, BYZT ceramics with $x = 0, 0.025$, and 0.05 were prepared by the solid-state reaction method at 1623 K ($1350 \text{ }^\circ\text{C}$) for 4 hours. XRD patterns and Rietveld refinement data confirmed that all BYZT ceramics have a perovskite-type cubic structure without

a deleterious phase. Structural refinement data facilitate the modeling of cuboctahedral $[\text{BaO}_{12}]$, octahedral $[\text{YO}_6]/[\text{TiO}_6]$, and $[\text{ZrO}_6]$ clusters in the BYZT lattice. Complex impedance plot samples confirmed both grain and grain boundary effects. Non-Debye-type relaxation in BYZT ceramics has been confirmed from the modulus analyses. All compositions show NTCR behavior which is required for highly sensitive thermistor applications. The nature of dc electric conductivity with temperature demonstrates that compounds exhibit an Arrhenius type of electric conductivity. The increase in ac conductivity leading to an increase in frequency indicates the existence of nonhomogeneities between grain and grain boundaries in BYZT ceramics as well as enhancement of mobile charge carrier through the grain boundary.

ACKNOWLEDGMENTS

The Brazilian authors acknowledge the financial support of the Brazilian research financing institutions: FAPESP-Postdoctoral (No. 2009/50303-4), CNPq (350711/2012-7), FAPEPI-GERATEC (No. 01.08.0506.00), and CAPES.

REFERENCES

1. Z. Yu, G. Ang, R. Guo, and A.S. Bhalla: *J. Appl. Phys.*, 2002, vol. 92, p. 1489.
2. S. Majan, O.P. Thakur, D. Bhattacharya, and K. Sreenivas: *J. Am. Ceram. Soc.*, 2009, vol. 92, p. 416.
3. Z. Yu, C. Ang, C.R. Guo, and A.S. Bhalla: *Mater. Lett.*, 2007, vol. 61, p. 326.
4. T. Maiti, R. Guo, and A.S. Bhalla: *Appl. Phys. Lett.*, 2006, vol. 89, p. 122909.
5. X.P. Jiang, M. Zeng, H.L.W. Chan, and C.L. Choy: *Mater. Sci. Eng. A*, 2006, vol. 438, p. 198.
6. T. Maiti, T.R. Guo, and A.S. Bhalla: *Appl. Phys. Lett.*, 2007, vol. 90, p. 182901.
7. R. Farhi, M. Marssi, A. Simon, and J. Ravez: *Eur. Phys. J. B*, 1999, vol. 9, p. 599.
8. T. Maiti, R. Guo, and A.S. Bhalla: *J. Am. Ceram. Soc.*, 2008, vol. 91, p. 1769.
9. T. Badapanda, S.K. Rout, L.S. Cavalcante, J.C. Sczancoski, S. Panigrahi, E. Longo, and M.S. Siu: *J. Phys. D*, 2009, vol. 42, p. 175414.
10. C. Ostos, L. Mestres, M.L. Martinez-Sarrion, J.E. Garcia, A. Albareda, and R. Perez: *Solid State Sci.*, 2009, vol. 11, p. 1016.
11. H.D. Kim and J.T. Song: *J. Ceram. Proc. Res.*, 2011, vol. 12, p. 322.
12. Y. Mizuno, Y. Okino, H. Chazono, and H. Kishi: *Jpn. J. Appl. Phys.*, 1998, vol. 37, p. 5227.
13. H. Kishi, N. Kohzu, J. Sugino, H. Ohsato, Y. Iguchi, and T. Okuda: *J. Eur. Ceram. Soc.*, 2001, vol. 21, p. 1643.
14. C.H. Kim, K.J. Park, Y.J. Yoon, M.H. Hong, J.O. Hong, and K.H. Hur: *J. Eur. Ceram. Soc.*, 2008, vol. 28, p. 1213.
15. Y. Sakabe, Y. Hamaji, H. Sano, and N. Wada: *Jpn. J. Appl. Phys.*, 2002, vol. 41, p. 5668.
16. H. Saito, H. Chazono, H. Kishi, and N. Yamaoka: *Jpn. J. Appl. Phys.*, 2001, vol. 30, p. 2307.
17. T. Badapanda, S.K. Rout, L.S. Cavalcante, J.C. Sczancoski, S. Panigrahi, T.P. Sinha, and E. Longo: *Mater. Chem. Phys.*, 2010, vol. 121, p. 147.
18. T. Badapanda, S.K. Rout, S. Panigrahi, T.P. Sinha, and S.I. Woo: *J. Korean Phys. Soc.*, 2009, vol. 55, p. 749.
19. T. Badapanda, S.K. Rout, S. Panigrahi, and T.P. Sinha: *Curr. Appl. Phys.*, 2009, vol. 9, p. 727.

20. S. Imashuku, T. Uda, Y. Nose, and Y. Awakura: *J. Alloys Compd.*, 2010, vol. 490, p. 672.
21. W.C. Yang, C.T. Hu, and I.N. Lin: *Ferroelectrics.*, 2002, vol. 270, p. 135.
22. O. Bidault, P. Goux, M. Kchikech, M. Belkaoumi, and M. Maglione: *Phys. Rev. B*, 1994, vol. 49, p. 7868.
23. W. Li, A.P. Chen, X.U. Lu, and J.S. Zhu: *J. Appl. Phys.*, 2005, vol. 98, p. 024109.
24. C. Ang, Z. Yu, and L.E. Cross: *Phys. Rev. B*, 2000, vol. 62, p. 228.
25. J.C. Sczancoski, L.S. Cavalcante, T. Badapanda, S.K. Rout, S. Panigrahi, V.R. Mastelaro, J.A. Varela, M.S. Li, and E. Longo: *Solid State Sci.*, 2010, vol. 12, p. 1160.
26. T. Badapanda, V. Senthil, S.K. Rout, L.S. Cavalcante, A.Z. Simoes, T.P. Sinha, S. Panigrahi, M.M. de Jesus, E. Longo, and J.A. Varela: *Curr. Appl. Phys.*, 2011, vol. 11, p. 1282.
27. J. Joseph, T.M. Vimala, J. Raju, and V.R.K. Murthy: *J. Phys. D*, 1999, vol. 32, p. 1049.
28. D. Shan, Y.F. Qu, and J.J. Song: *Solid State Commun.*, 2007, vol. 141, p. 65.
29. S.R. Hall, F.H. Allen, and I.D. Brown: *Acta Crystallogr. A*, 1991, vol. 47, p. 655.
30. L. Lutterotti, S. Matthies, and H.R. Wenk: MAUD: A friendly Java Program for Material Analysis Using Diffraction, IUCr: newsletter of the CPD, 1999, vol. 21, p. 14.
31. L. Lutterotti, S. Matthies, H.R. Wenk, A.J. Schultz, and J. Richardson: *J. Appl. Phys.*, 1997, vol. 81, p. 594.
32. L. Cont, D. Chateigner, L. Lutterotti, J. Ricote, M.L. Calzada, and J. Mendiola: *Ferroelectrics*, 2002, vol. 267, p. 323.
33. L. Lutterotti, M. VoLtoLini, H.R. Wenk, K. Bandyopadhyay, and T. Vanorio: *Am. Miner.*, 2010, vol. 95, p. 98.
34. G. Will: *Powder Diffraction: The Rietveld Method and the Two Stage Method to Determine and Refine Crystal Structures from Powder Diffraction Data*, Springer, Berlin, 2006, p. 44.
35. H.H. Huang, H.H. Chiu, N.C. Wu, and M.C. Wang: *Metall. Mater. Trans. A*, 2008, vol. 39A, p. 3276.
36. F.A. Rabuffetti and R.L. Brutchey: *Chem. Commun.*, 2012, vol. 48, p. 1437.
37. N. Jiang, D. Su, and J.C.H. Spence: *Phys. Rev. B*, 2007, vol. 76, p. 214117.
38. T. Maiti, E. Alberta, R. Guo, and A.S. Bhalla: *Mater. Lett.*, 2006, vol. 60, p. 3861.
39. T. Maiti, R. Guo, and A.S. Bhalla: *J. Appl. Phys.*, 2006, vol. 100, p. 114109.
40. C. Duan, J. Yuan, and J. Zhao: *J. Solid State Chem.*, 2005, vol. 178, p. 3698.
41. P. Petkov, I. Iliev, T. Petkova, and V. Vassilev: *J Optoelectron Adv Mater*, 2003, vol. 5, p. 521.
42. A.K. Jonascher: *Nature*, 1977, vol. 267, p. 673.
43. A. Lasia: in *Modern Aspects of Electrochemistry*, B.E. Conway, J.O.M. Bockris, and R.E. White, eds., Kluwer Academic/Plenum Publishers, New York, 1999, p. 143.
44. M. Guillodo, J. Fouletier, L. Dessemond, and P. Del Gallo: *J. Eur. Ceram. Soc.*, 2001, vol. 21, p. 2331.
45. M.A.L. Nobre and S. Lanfredi: *Appl. Phys. Lett.*, 2002, vol. 81, p. 451.
46. S. Lanfredi and M.A.L. Nobre: *Appl. Phys. Lett.*, 2005, vol. 86, p. 081916.
47. K. Park: *J. Am. Ceram. Soc.*, 2005, vol. 88, p. 862.
48. A. Feteira: *J. Am. Ceram. Soc.*, 2009, vol. 92, p. 967.
49. R. Sagar, P. Hudge, S. Madolappa, A.C. Kumbharkhane, and R.L. Raibagkar: *J Alloys Compd*, 2012, vol. 537, p. 197.
50. J.R. Macdonald: *Impedance Spectroscopy: Emphasizing Solid State Material and Sytems*, Wiley, New York, 1987.
51. P.B. Macedo, C.T. Moynihan, and R. Bose: *Phys. Chem. Glasses*, 1972, vol. 13, p. 171.
52. W. Cao and R. Gerhardt: *Solid State Ionics.*, 1990, vol. 42, p. 213.
53. F. Argall and A.K. Jonscher: *Thin Solid Films*, 1968, vol. 2, p. 185.
54. T.C. Chen, C.L. Thio, and S.B. Desu: *J. Mater. Res.*, 1997, vol. 12, p. 2628.